Qin *et al. Microstructures* **2025**, *5*, 2025022
**DOI:** 10.20517/microstructures.2024.70

**Microstructures**

**Research Article**

**Open Access**

Check for updates

# Oxygen coordinated Cu single atom catalysts: a superior catalyst towards electrochemical $CO_2$ reduction for methane production

**Jundi Qin[#], Xiao Hu[#], Kanghua Miao, Xiongwu Kang**

School of Environment and Energy, South China University of Technology, Guangzhou 510006, Guangdong, China.
[#]Authors contributed equally.

**Correspondence to:** Prof. Xiongwu Kang, School of Environment and Energy, South China University of Technology, 382 East Waihuan Road, Higher Education Mega Center, Guangzhou 510006, Guangdong, China. E-mail: esxkang@scut.edu.cn

**How to cite this article:** Qin, J.; Hu, X.; Miao, K.; Kang, X. Oxygen coordinated Cu single atom catalysts: a superior catalyst towards electrochemical $CO_2$ reduction for methane production. *Microstructures* **2025**, *5*, 2025022. https://dx.doi.org/10.20517/microstructures.2024.70

**Received:** 5 Aug 2024 **First Decision:** 6 Sep 2024 **Revised:** 22 Sep 2024 **Accepted:** 15 Oct 2024 **Published:** 25 Feb 2025

**Academic Editors:** Dingsheng Wang, Zaiping Guo **Copy Editor:** Ping Zhang **Production Editor:** Ping Zhang

## Abstract

Single atom catalyst (SAC) show significant promise in electrocatalytic carbon dioxide reduction reaction ($eCO_2RR$) to produce valuable chemicals, representing one of the most promising ways to achieve a carbon neutral cycle. Methane is one of the many valuable products from $eCO_2RR$. Rational design of SAC through deliberate coordination regulation and controlled synthesis at low temperatures toward methane production remains very limited. Herein in this paper, Cu SAC with coordination of four oxygen atoms ($Cu\text{-}O_4$) were prepared by soaking Cu nanocrystals on carbon support in acetic acid solution at 60 °C for 12 h. The coordination structure was revealed by extended X-ray absorption fine structure spectrum and X-ray photoelectron spectroscopy. $Cu\text{-}O_4$ SAC demonstrates excellent activity and selectivity towards methane production, with a Faradaic efficiency (FE) of 63.0% and partial current density of 200.5 mA $cm^{-2}$. Theoretical calculation indicates less positive charge of Cu center and stronger charge delocalization in $Cu\text{-}O_4$ SAC than $Cu\text{-}N_4$ SAC due to the stronger $\pi$ bonding interaction in $Cu\text{-}O_4$ SAC, which stabilizes the methane intermediates and lowers the potential determining step on $Cu\text{-}O_4$ SAC. Strong hydrogen adsorption on $Cu\text{-}O_4$ SAC suppresses hydrogen evolution and may favor hydrogenation of reaction intermediates to methane. The limiting potential indicates that methane is more favored on $Cu\text{-}O_4$ SAC than CO, methanol and formate, corroborating the high selectivity of methane production on $Cu\text{-}O_4$ SAC. This work highlights the importance of regulation of the coordination environment in SAC in steering products in $eCO_2RR$.

**Keywords:** Single atom catalyst, oxygen coordination, charge delocalization, $CO_2$ reduction

## INTRODUCTION

Electrocatalytic carbon dioxide reduction ($eCO_2RR$) can produce valuable chemicals and fuels[1], such as carbon monoxide, methane, formic acid, methanol, ethylene, ethanol, *etc.*[2-7], and represents one of the most promising ways to achieve a carbon neutral cycle[8,9]. Among the many valuable products, methane ($CH_4$), with an energy density of 55.5 MJ $kg^{-1}$, is attractive for a wide range of energy applications. Efficient conversion of $CO_2$ to $CH_4$ not only addresses environmental concerns but also provides a sustainable energy resource compatible with existing natural gas infrastructure.

Single atom catalyst (SAC), featured by maximum atom utilization, well-defined active sites, and unique electronic and geometrical structures, have been widely studied as $eCO_2RR$ catalysts[10-13]. Previous studies have demonstrated that the coordination environment around the Cu atoms plays a crucial role in determining the activity and selectivity of SAC. For instance, Cu SAC coordinated with carbon atoms (Cu-C) on graphyne substrates favor the formation of *OCHO intermediates, leading to dominant methane production in $eCO_2RR$[14]. The selectivity toward $CH_4$ can also be regulated by adjusting the spacing of adjacent metal active sites, which influences reaction pathways and intermediate stabilizatio[15].

Moreover, heteroatom doping in the coordination shells of SAC provides an effective strategy to precisely regulate their electronic structure and catalytic activity[16,17]. It is reported that Cu SAC coordinated with two N-atom ($Cu-N_2$) in the first shell shows impressive catalytic activity in $eCO_2RR$ towards formation of ethanol[18]. However, O coordination results in lower charge density of metal center due to the higher electron negativity than N, and O-heteroatom doping into the N-coordination may induce apparent regulation towards electronic structure of metal center and the N, O co-coordinated Cu SAC ($Cu-N_2O_2$) exhibits remarkably high activity and selectivity of methane production[19]. Doping of coordination with other nonmetal elements with higher electronegativity than nitrogen equally promotes $eCO_2RR$ towards methane production. For instance, B-doping into the Cu-N coordination in the first shell of Cu SAC ($Cu-N_2B_2$) promotes the adsorption of *CO and *CHO intermediates and demonstrates a current density of 462 mA $cm^{-2}$ and Faradaic efficiency (FE) of 73% for methane production in $eCO_2RR$[20].

Despite the promising performance of SAC, the green synthesis of these catalysts remains a critical task. The methods for synthesis of SAC have evolved from traditional techniques such as impregnation, mass-selected soft landing, and co-precipitation to emerging approaches such as atomic layer deposition[21], host-guest strategies[22], and photochemical synthesis[23]. Currently, most of the reported SAC were fabricated by thermal annealing method at high temperatures[9], which results in diverse structure of SAC sites and makes it difficult to establish a structure-activity relationship. Additionally, aggregation of metal atoms results in formation of metal nanoclusters and intensive acid etching is always inevitable to remove the metal nanoclusters and reserve SAC only[24]. Furthermore, in some cases, metal nanoclusters were confined in carbon nanotubes and were very challenging to be removed by acid etching, and thermal annealing in ammonium atmosphere is required[11]. Therefore, this conventional thermo-anneal method at high temperatures is energy-intensive and not suitable for commercial applications[25]. Therefore, it is imperative to develop low temperature method for structure-controlled synthesis of SAC in terms of energy efficiency and environmental friendliness.

Herein, Cu SAC with coordination of four O atoms ($Cu-O_4$) were prepared by three sequential steps: soaking of XC-72 in aqua regia to create defects and oxygenated functional groups, growth of copper cubes on treated XC-72 at 120 °C, soaking of the sample in acetic acid for dissolution of Cu atoms from Cu cube and deposition Cu single atoms on defects of oxygenated functional groups on carbon substrate. The unique coordination environment and spread of Cu single atoms were evidenced by high-resolution transmission

electron microscopy (HR-TEM) and extended X-ray absorption fine structure (EXAFS). Cu-$O_4$ SAC, as e$CO_2$RR catalyst on a gas diffusion electrode (GDE) and flow cell setup, demonstrate an FE of 63.0% and a current density of 200.5 mA $cm^{-2}$. Density functional theory (DFT) calculation indicates that methane production is more favored energetically than that on Cu-$N_4$ SAC and the Cu(111) of copper nanoparticles (CuNPs), which is attributed to the optimized electronic structure and preferred adsorption of the reaction intermediates of methane on Cu-$O_4$ SAC.

## MATERIALS AND METHODS

### Chemicals

Copper (II) chloride ($CuCl_2·2H_2O$), absolute ethanol ($C_2H_5OH$, 99%), glucose (99%), toner (XC-72), acetic acid (97%) were purchased from Damao Chemical Reagent. Hexadecylamine (HAD, 97%) was purchased from Energy Chemical (China). $CO_2$ (99.995%), Ar (purity 99.99%), $N_2$ (purity, 99.99%) and $H_2$ (purity 99.99%) were purchased from Messer Gas (Guangzhou, China). All chemicals were used without any further purification and all solutions were prepared using deionized (DI) water (18.2 MΩ cm).

### Materials synthesis

*Pretreatments of XC-72*

First, 10 g of XC-72 carbon material was added to a mixture of 225 mL concentrated hydrochloric acid and 75 mL concentrated nitric acid. After oxidizing for a specified duration, the resulting slurry was cooled, centrifuged, and repeatedly washed with water and ethanol until the pH reached neutral. The sample was then dried overnight at 60 °C in a vacuum oven.

*Synthesis of Cu/C*

XC-72 supported Cu cube (Cu/C) was synthesized according to a slightly modified version of a previously reported method[26]. In general, $CuCl_2$-$2H_2O$ and glucose were dissolved in 80 mL of water, and after complete dissolution, XC-72 toner was added by magnetically stirring at room temperature for 5 h. HAD (1.44 g) was slowly added during this process. After forming a light blue emulsion, it was poured into the Teflon-lined chamber and heated at 120 °C for 2 h under vigorous magnetic stirring. As the reaction proceeded, the solution changed its color from blue to brown and finally red-brown. After cooling to room temperature, the samples were washed several times with DI water and ethanol to obtain the Cu/C catalyst.

*Synthesis of Cu SAC*

First, 70 mg of Cu/C was dispersed in a solution of acetic acid and ethanol in a volume ratio of 1:1 to remove the excess HAD organic ligand and form Cu SAC on XC-72 by acid etching. Cu SAC was obtained by centrifugation and washing several times with DI water and ethanol, and then drying for 12 h at 60 °C.

### Electrode preparation

The carbon paper was cut into sheets (2.5 × 1 $cm^2$). The catalyst was dispersed in a solution of water isopropyl alcohol and Nafion ($V_{water}$: $V_{isopropyl\ alcohol}$: $V_{Nafion}$ = 1:1:0.025) to form a catalyst ink (7.5 mg $mL^{-1}$) by ultrasonication for one hour. The uniformly dispersed catalyst droplets were coated on a piece of the carbon paper (Sigracet 29 BC from Fuel Cell Store) with a microporous acetylene black gas diffusion layer (GDL) on the other side (2 × 0.5 $cm^2$ for geometric electrode surface area). The catalyst loading on the carbon paper is at 1.0 mg $cm^{-2}$.

### Electrochemical test

Electrochemical measurements were conducted using the CHI 760D Electrochemical Station (Chenhua Shanghai, China). $CO_2$ electrochemical reduction experiments were performed in a custom-designed flow cell with a Pt sheet as the anode and the catalyst-coated carbon paper as the cathode, separated by an anion

exchange membrane (Selemion, 2 × 1.5 $cm^2$). Hg/HgO electrodes served as reference electrodes. All applied potentials were referenced to the reversible hydrogen electrode (RHE) based on

$$E\ (vs.\ \text{RHE}) = E\ (vs.\ \text{Hg / HgO}) + 0.098V + 0.0591 \times pH \quad (1)$$

During electrochemical measurement, $CO_2$ was purged into the GDL at a flow rate of 24 mL $min^{-1}$ while electrolyte (1 M Ar-saturated KOH) was delivered to the flow cell at 120 rpm using a peristaltic pump. Electrochemical impedance spectroscopy (EIS) tests were carried out at an applied potential of -0.9V (RHE), a voltage amplitude of 5 mV and a frequency range (0.1 Hz to 100 kHz).

The electrochemical surface area (ECSA) of the catalysts was determined using electrochemical double layer capacitance ($C_{dl}$), as given in

$$\text{ECSA} = \frac{S * C_{dl}}{C_s} \quad (2)$$

where $C_{dl}$ is the double layer capacitance, $S$ is the geometric area of the working electrode (1 $cm^2$), and $C_s$ is the specific capacitance of the carbon-based support (0.020 mF $cm^{-2}$).

The FE for the products was calculated using

$$\text{FE} = \frac{Q_i}{Q_t} = \frac{nN_iF}{Q_t} \quad (3)$$

where $Q_t$ (C) is the total charge collected at the applied potential, $Q_i$ (C) represents the total charge to produce the certain product, n is the number of electrons transferred for the product, which is 2 for both CO and $H_2$, and 8 for $CH_4$, 12 for $C_2H_4$, $N_i$ is the number of moles of the certain product, and F stands for Faraday's constant, which has a value of 96,485 C $mol^{-1}$.

### Characterization

Using the JEOL ARM200F instrument (JEOL, Tokyo, Japan), the dispersion state of copper species was characterized by aberration-correction high-angle-annular-dark-field scanning transmission electron microscopy (AC-HAADF-STEM). X-ray diffraction (XRD) spectroscopy was acquired on D8-Advance (BRUKER-AXS, German) system at a scan rate of 5 degrees·$min^{-1}$ to analyze the crystalline structure. The composition and chemical states of the elements were analyzed via X-ray photoelectron spectroscopy (XPS). The metal loading in the Cu SAC was quantified by inductively coupled plasma atomic emission spectrometry (ICP-AES).

### Synchrotron radiation-based X-ray absorption spectroscopy

The X-ray absorption fine structure (XAFS) spectrum of Cu K-edge (8,979 eV) was obtained using a fluorescence mode on the BL14W1 beamline at the Synchrotron Radiation Facility (SSRF) in Shanghai, China. The storage ring of the device operates at a beam current of 3.5 GeV and 230 mA. The beamline beam was monochromatized using a double-crystal monochromator (DCM) equipped with Si (111) crystals. All XAFS spectra were analyzed using the Demeter software package (University of Chicago).

Normalization of X-ray absorption near edge structure raw data

First, the photon energy was calibrated by referencing the Cu 4f peak of a newly sputtered Cu wafer, ensuring accurate energy measurement by XAFS. Subsequently, the front edge of the Cu K-edge spectrum was set to zero using substrate lines to establish a consistent baseline reference for further analysis. Finally, the spectrum was normalized to achieve an edge-jump of one. In the fitting process, the theoretical curve-wave backscattering amplitude [Fj(k)], phase-shift function [j(k)], and mean free path Å(l) were calculated for all paths using the FEFF8.2 code (University of Washington). Incorporating these calculated values into the fitting model allowed for the analysis and interpretation of the experimental XAFS spectra in terms of the local atomic structure and electronic properties of the sample.

### Computational details

All DFT calculations in this paper have been performed using the pseudopotential plane wave (PP-PW)-based Cambridge Sequence Total Energy Package (CASTEP)[27] module of BIOVIA Corporation, which is the version of Material Studio R17.2. Exchange-correlation interactions are handled by Perdew-Burke-Ernzerhof (PBE) functions at the Generalized Gradient Approximation (GGA) level[28,29], and ultrasoft pseudopotentials are used to describe the interactions between ionic nuclei and valence electrons[30]. The Brillouin zone for the optimized catalyst structure was sampled using a 3 × 3 × 1 Monkhorst-Pack k-point mesh. For the Cu (111) substrate, a 4 × 4 × 4 periodic cell was used, with the bottom atomic layer fixed during surface adsorption calculations. For the monatomic Cu catalyst, a monolayer graphene surface with Cu single atoms anchored on defects and coordinated with four oxygen atoms. The vacuum layer was set to 15 Å to avoid the effects of periodicity. A plane-wave basis set with a cutoff energy of 400 eV was used to expand the electronic wave function. The convergence criteria for the electron self-consistent iteration and the force were set to $10^{-5}$ eV and 0.03 eV $Å^{-1}$, respectively. All adsorption energies ($\Delta E$) were calculated using

$$\Delta E = E_{\text{adsorbate+substrate}} - E_{\text{adsorbate}} - E_{\text{substrate}} \tag{4}$$

where $E_{\text{adsorbate+substrate}}$, $E_{\text{adsorbate}}$, and $E_{\text{substrate}}$ are the total energies optimized for adsorbent + substrate, substrate alone, and gas-phase adsorbent, respectively.

The Gibbs free energy ($\Delta G$) of the reaction was calculated using[31]

$$\Delta G = \Delta E + \Delta ZPE - T\Delta S \tag{5}$$

$\Delta G$, $\Delta ZPE$, and $\Delta S$ denote the Gibbs free energy, the zero point energy, and the entropy, respectively.

The formation energy ($E_f$) serves as a metric to unveil the thermodynamic stability of all catalysts, computed as follows[32]:

$$\Delta E_f = E_{\text{substrate}} + n_C\mu_C - n_O\mu_O - \mu_{Cu} - E_{graphene} \tag{6}$$

$n_C$ and $n_O$ represent the quantities of C and O atoms introduced or extracted during substrate formation, $\mu_C$, $\mu_O$, and $\mu_{Cu}$ represent the chemical potentials of C, O, and Cu elements, respectively. The values of $\mu_C$, $\mu_O$, and $\mu_{Cu}$ are one in sixteen the energies of 4 × 4 perfect graphene, half energy of the $O_2$ molecules in the gaseous phase, and isolated Cu single atoms, respectively.

The limiting potential ($U_L$) represents the minimum applied potential necessary to ensure each elementary step in the proposed mechanism is exergonic. $U_L$ can be determined using[33]

$$U_L = -\Delta G_{MAX}/e \quad (7)$$

where $\Delta G_{MAX}$ denotes the free-energy change for the potential determining step along each $eCO_2RR$ pathway.

## RESULTS AND DISCUSSION

The Cu SAC was synthesized through acid leaching of Cu nanocrystals, as depicted in Figure 1A. Initially, Cu nanocrystals were uniformly prepared onto the carbon substrate (Cu/C) via a hydrothermal method[26,34]. Subsequently, the Cu/C catalysts were immersed in a mixed solution of ethanol-acetate (v:v = 1:1) at 60 °C with magnetic stirring for four h. This process aimed to dissolve Cu nanocrystals and produce uniformly distributed Cu single atoms on the defects of carbon substrate, which was treated by nitric acid/hydrochloric acid and possessing plenty of oxygen functional groups, such as C-O-C, to capture Cu atoms[35].

As shown in Figure 1B, scanning electron microscopy (SEM) images of Cu/C exhibit a majority of Cu nanocrystals and minority of Cu nanowires, which was completely dissolved by acetic acid leaching, as evidence by SEM and transmission electron microscopy (TEM) image [Figure 1C and D]. An AC-HAADF-STEM image indicates plenty of bright spots, which are ascribed to the atomically dispersed Cu sites [Figure 1E][36]. Additionally, high-angle-annular-dark-field scanning transmission electron microscopy (HAADF-STEM) illustrates the amorphous carbon nature of the material. Elemental mapping confirms the uniform distribution of Cu elements on Cu SAC [Figure 1F and G], corroborating the uniform distribution of atomically distributed Cu atoms.

The powder XRD of Cu/C reveals three diffraction peaks of Cu (111), Cu (200), and Cu (220) [Supplementary Figure 1], which were completely gone for Cu SAC sample after acid leaching. Inductively coupled plasma mass spectrometry (ICP-MS) indicates that the loading of Cu element in the catalyst is 0.45 wt%.

A comprehensive analysis of the XPS spectra for the elements Cu, C, and O was conducted to probe the bonding and chemical states of these elements in both the Cu SAC and Cu/C. Figure 2A depicts the Cu 2p XPS spectra of Cu/C and Cu SAC. Specifically, the two red dashed lines at 932.2 eV and 952.0 eV are associated with the binding energy of $2p^{3/2}$ and $2p^{1/2}$ of $Cu^+/Cu^0$, while the black dashed lines at 935.2 eV and 954.7 eV correspond to $2p^{3/2}$ and $2p^{1/2}$ of $Cu^{2+}$[37], indicating that Cu/C is dominated by metallic states with a slight degree of oxidation. However, the binding energy of Cu SAC $Cu2p^{1/2}$ and $Cu2p^{3/2}$ was positively shifted to 952.6 eV and 932.7 eV, which are positioned between $Cu^{2+}$ and $Cu^0$, suggesting a charge state of $Cu^{+\delta}$ between 0 and 2+ upon coordination with O atoms.

The C 1s XPS of Cu/C displays C-O (286.2 eV), C=C (284.8 eV) and C-C (285.5 eV)[37-39] and an extra subtle peak emerges at 288.8 eV for Cu SAC [Supplementary Figure 2], which are indexed to the COOH of acetate functionalization on Cu SAC due to acetate acid treatment. Likewise, the O 1s XPS spectrum of Cu SAC in Figure 2B displays peaks of O-Cu (531 eV), O=C (532 eV), and O-C (533 eV) bonds[40], with a slight additional O-Cu peak compared to the Cu/C catalyst [Supplementary Figure 3]. This suggests potential bonding between Cu and O in Cu SAC.

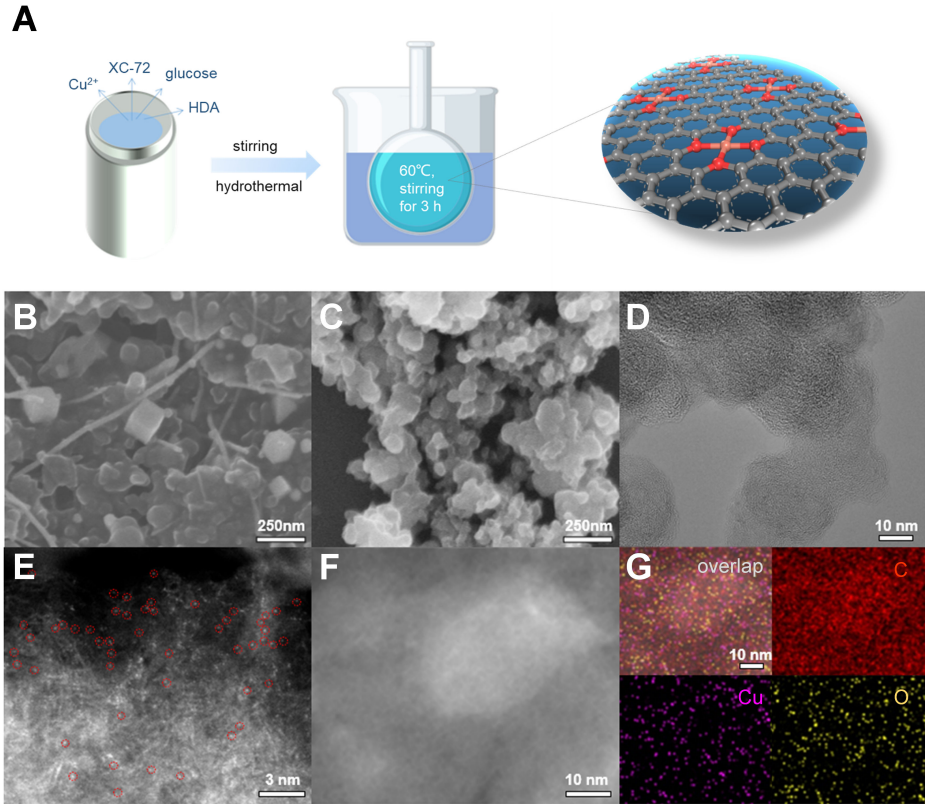


**Figure 1.** (A) Schematic illustration of the synthesis of the Cu SAC; SEM image of (B) Cu/C and (C) Cu SAC; (D) HR-TEM and (E) AC-HAADF-STEM image of Cu SAC; (F) HAADF-STEM, and (G) element mapping image of Cu SAC. SAC: Single atom catalyst; SEM: scanning electron microscopy; AC-HAADF-STEM: aberration-correction high-angle-annular-dark-field scanning transmission electron microscopy; HR-TEM: high-resolution transmission electron microscopy.

The investigation into the electronic structure and coordination of Cu species within the catalyst involves X-ray absorption near edge structure (XANES) and EXAFS analyses. The XANES of Cu SAC is very close to that of CuO and copper phthalocyanine (CuPc) [Figure 2C], which suggests a valence state of the Cu in Cu SAC proximate to +2, consistent with the XPS results[41]. However, the slightly less positive XANES of Cu SAC than that of CuPc suggests stronger electron donation by O-coordination than N-coordination due to $\pi$ bonding interaction.

In the EXAFS spectra [Figure 2D], the Cu SAC exhibits a peak at 1.5 Å, similar to those observed in CuPc and CuO, indicating the possible Cu-N/O coordination. No apparent Cu-Cu coordination for Cu SAC at 2.2 Å demonstrates the atomic dispersion of the Cu atoms, consistent with the results observed by AC HAADF STEM and XRD. The coordination surroundings of Cu SAC were analyzed the numerical fitting of EXAFS using the real-space multiple scattering algorithm implemented in the FEFF9 program[42] [Figure 2E], which demonstrates a coordination number of 3.9 for Cu-N/O coordination [Supplementary Table 1]. To further identify the exact Cu-N/O coordination in Cu SAC, formation energy of $Cu\text{-}N_xO_{4-x}$ (x = 1 - 4) configurations was further explored by DFT calculation [Figure 2F][32]. It was observed that the formation energy of $Cu\text{-}O_4$ configuration shows the lowest formation energy (-0.84 eV) among the five configurations, confirming the $Cu\text{-}O_4$ configuration in Cu SAC.

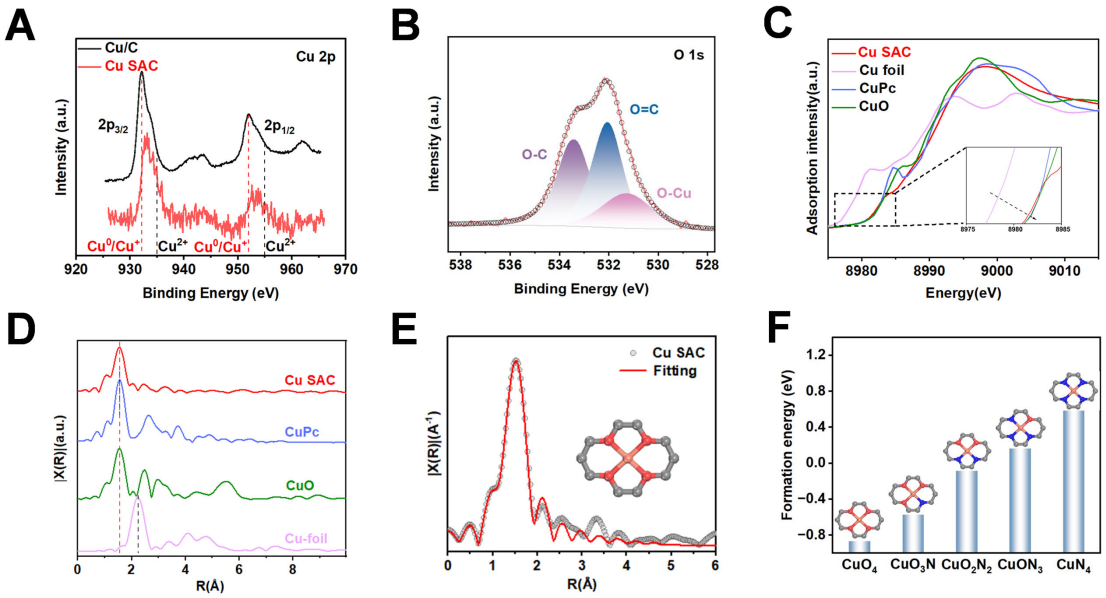


**Figure 2.** XPS spectra of (A) Cu 2p; (B) O 1s for Cu SAC; (C) Normalized Cu K-edge XANES spectra; (D) FT-EXAFS spectra of Cu SAC; (E) EXAFS fitting and (inset) optimized model for Cu SAC; (F) Formation energy of Cu-$N_xO_{4-x}$ (x=0-4) configurations with the coordination number of first-shell N/O species from DFT calculations. Color scheme: C atoms are grey, O atoms are red, N atoms are blue, and Cu atoms are orange. XPS: X-ray photoelectron spectroscopy; SAC: single atom catalyst; XANES: X-ray absorption near edge structure; EXAFS: extended X-ray absorption fine structure; DFT: density functional theory; FT-EXAFS: fourier transforms of extended X-ray absorption fine structure.

The activity and selectivity of $eCO_2RR$ on Cu-$O_4$ SAC and Cu/C catalysts were evaluated in a flow cell setup with a GDE and 1 M KOH electrolyte, covering the potential range from -0.7 to -1.1 V *vs.* RHE. The 1 M KOH electrolyte provides a high concentration of $OH^-$ ions, suppressing the competing hydrogen evolution reaction (HER), while ensuring sufficient $OH^-/e^-$ participation in $CO_2$ reduction to $CH_4$. High concentration of KOH may promote the formation of C-C coupled multi-carbon products[43]. The GDE improves $CO_2$ and catalyst accessibility, while the flow cell overcomes mass transfer limitations typical of traditional systems by creating a three-phase interface, facilitating efficient interaction between gas reactants and the catalyst-electrolyte interface, thereby increasing the maximum current density[44]. Besides, the hydrophobic nature of the carbon paper helps suppress HER on the catalyst surface. Then, product quantification from $eCO_2RR$ was performed using $^1$H nuclear magnetic resonance ($^1$H-NMR) and gas chromatography (GC). As shown in Figure 3A-D, Cu-$O_4$ SAC achieves an FE of 63.0% towards methane production and a maximum partial current density of 200.5 mA $cm^{-2}$ at -1.0 V *vs.* RHE, while $C_2H_4$ selectivity is 2.2%. The activity and selectivity for methane production on Cu-$O_4$ SAC is much higher than that on Cu/C catalyst, which displays an FE of 13.9% for $C_2H_4$, 33.2% for $CH_4$ and 45.3% for HER. These findings highlight the superior catalytic performance and selectivity of Cu-$O_4$ SAC for $eCO_2RR$ towards methane. The enhanced activity and selectivity of the Cu-$O_4$ SAC can be attributed not only to the unique O-coordination Cu SAC structure but also to the optimized reaction conditions and electrolyte environment.

The prevailing understanding posits that the formation of $C_2H_4$ entails a C-C coupling process facilitated by adjacent Cu atoms on the crystal surfaces, a mechanism often referred to as the Langmuir-Hinshelwood (LH) mechanism[45]. Within this framework, SAC demonstrate a unique ability to suppress the C-C coupling reactions of multi-carbon ($C_{2+}$) products due to their singular adsorption sites, thereby enhancing selectivity towards $C_1$ products[46,47]. Notably, Cu-$O_4$ SAC catalyst [Figure 3E] remains stable in ten hours of

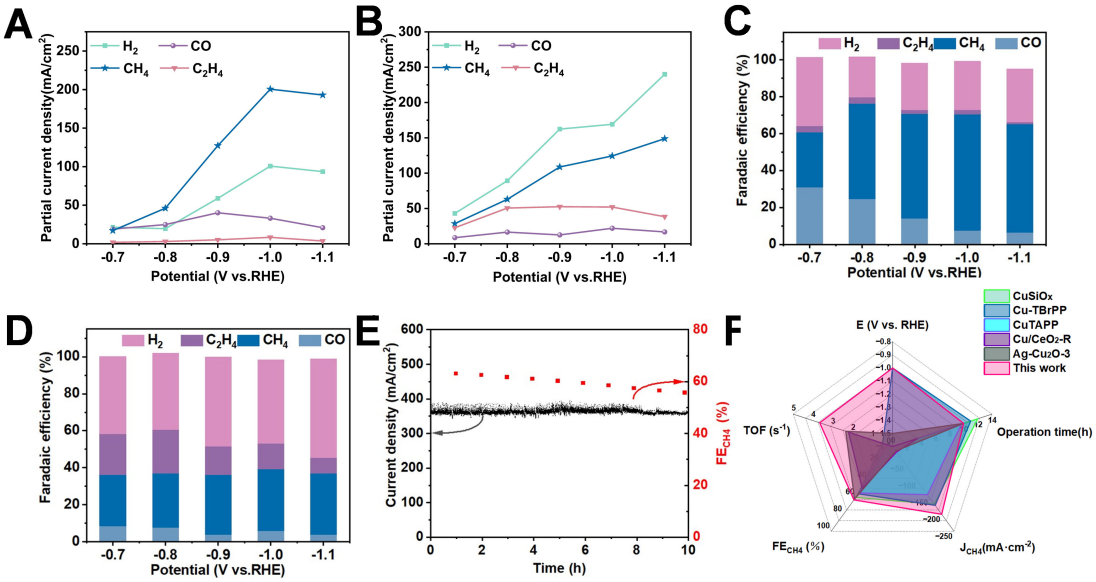


**Figure 3.** $eCO_2RR$ performance: partial current density on (A) Cu-$O_4$ SAC and (B) Cu/C at varying applied potentials; FE of various $eCO_2RR$ products on (C) Cu-$O_4$ SAC and (D) Cu/C; (E) Stability test of Cu-$O_4$ SAC at -1.0 V; (F) Comparison of performance indexes of $eCO_2RR$ to $CH_4$ with reported catalysts. $eCO_2RR$: Electrocatalytic carbon dioxide reduction; SAC: single atom catalyst; FE: faradaic efficiency; $CH_4$: methane.

$eCO_2RR$ at -1.0 V *vs.* RHE, with FE over 50% and a partial current density of approximately 150 mA $cm^{-2}$ for methane production. Cu SAC show exceptional catalytic performance for $CO_2$-to-$CH_4$ electroreduction as compared to those reported in the literature [Figure 3F, Supplementary Table 2].

The charge transfer characteristics of the catalyst were studied by Nyquist analysis. Typically, electrochemical processes at the electrode surface are controlled by interfacial charge transfer and diffusion processes on planar electrodes. The semi-circle in the high-frequency region of the Nyquist diagram usually reflects the interfacial charge transfer resistance[48]. As shown in Supplementary Figure 4, the interfacial charge transfer ($R_{ct}$) of Cu-$O_4$ SAC catalyst is almost half that of Cu/C, indicating a much faster $eCO_2RR$ process on Cu-$O_4$ SAC.

In order to further study the intrinsic activity of the catalyst, the ECSA of the catalyst was determined by using double-layer capacitance ($C_{dl}$) [Supplementary Figure 5]. As shown in Supplementary Table 3, the ECSA of Cu-$O_4$ SAC is 0.24 $cm^2$, which is significantly smaller than that of Cu/C (0.64 $cm^2$). Such reduction of the surface area of Cu-$O_4$ SAC is mainly due to the dissolution of the Cu nanoparticles after acid leaching. When normalized to ECSA, the partial current of $CH_4$ at each potential of Cu-$O_4$ SAC is much higher than that of Cu/C [Supplementary Figure 6] in the potential range of -0.7V to -1.1 V (*vs.* RHE), indicating its high intrinsic activity towards $eCO_2RR$ for methane production.

Fully elucidating the superior activity and selectivity of Cu-$O_4$ towards methane production, DFT calculations were employed to investigate the energetics of the $eCO_2RR$ reaction pathway[49-51]. The adsorption configurations of the $eCO_2RR$ intermediates on Cu-$N_4$ and Cu-$O_4$ SAC [Supplementary Figures 7-9] show that the Cu-$O_4$ coordination dynamically converts to Cu-$O_2$ and Cu-O coordination upon adsorption of $eCO_2RR$ intermediates. However, Cu-$N_4$ coordination with most of the $eCO_2RR$ intermediates remains intact. Such variation of the configuration of the Cu-$N_4$ SAC and Cu-$O_4$ SAC structure might be responsible for the significantly lower energetic of the $eCO_2RR$ intermediates to

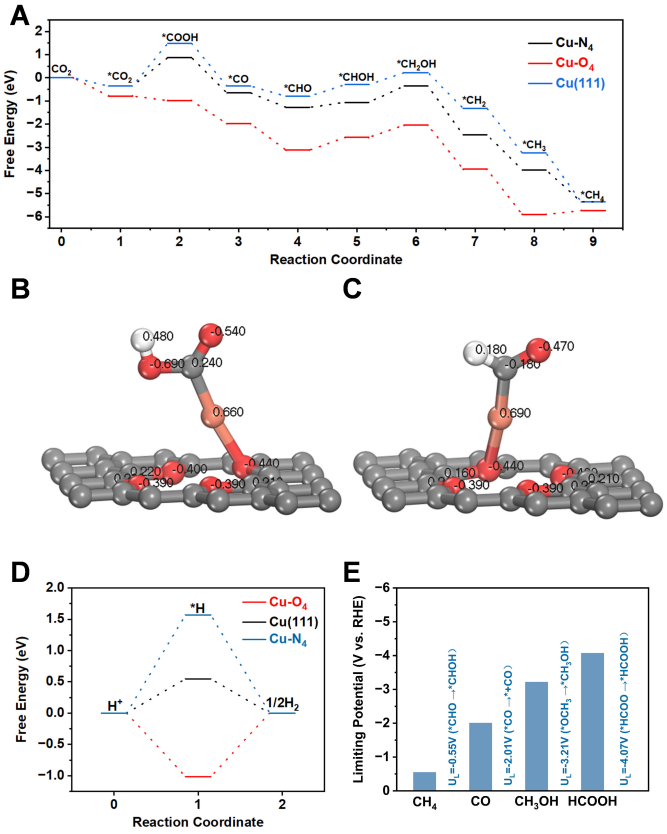


**Figure 4.** Evaluation of catalytic activity by DFT simulations. (A) Free energy diagram of $eCO_2RR$ pathway to $CH_4$; Bader charge of (B) Cu-$O_4$ and (C) Cu-$N_4$ SAC; (D) $\Delta G_H$ on Cu-$O_4$ SAC, Cu (111), Cu-$N_4$ SAC; (E) Limiting potentials of $CH_4$, CO, $CH_3OH$ and HCOOH on Cu-$O_4$ SAC. DFT: Density functional theory; $eCO_2RR$: Electrocatalytic carbon dioxide reduction; $CH_4$: Methane; SAC: single atom catalyst.

methane on Cu-$O_4$ SAC than Cu-$N_4$ SAC and Cu (111) surface in Figure 4A. Meanwhile, the potential-determining step (PDS) is *CHO+($H^+$+$e^-$) → *CHOH, with an energy barrier of 0.55 eV for Cu-$O_4$ SAC. The PDS is *$CO_2$+($H^+$+$e^-$) → *COOH on both Cu-$N_4$ SAC and Cu (111), with an energy barrier of 1.86 eV and 1.23 eV, respectively. The PDS on Cu-$O_4$ SAC exhibits an obvious lower energy barrier than Cu (111) and Cu-$N_4$ SAC, corroborating the superior activity of $eCO_2RR$ towards methane on Cu-$O_4$ SAC.

The Bader charge was further calculated to gain deeper insight into the variation of the electronic structure induced by O-coordination and potential interaction on the adsorption of $eCO_2RR$ intermediates[52]. As shown in Figure 4B and C, Supplementary Figure 10, the Bader charge analysis reveals that as the number of coordinating oxygen atoms increases, the positive charge on Cu gradually decreases from +1.43 for $CuN_4$ SAC to +1.15 for Cu-$O_4$ SAC, indicating enhanced charge delocalization in Cu-$O_4$ SAC than Cu-$N_4$ SAC structure. This might be responsible for the further dynamic partial cleavage of the Cu-O bonds in Cu-$O_4$ SAC upon adsorption of $eCO_2RR$ intermediates. The differential charge density of Cu in Cu-$O_4$ SAC indicates less positive charge than that of Cu in Cu-$N_4$ SAC structure [Supplementary Figure 11]. The less positive valence state of Cu in Cu-$O_4$ SAC than Cu-$N_4$ SAC aligns with observations from XPS and EXAFS. Similar results were observed for Cu-$O_4$ and Cu-$N_4$ with adsorbed *COOH and *CHO intermediates [Supplementary Figures 12-14][52].

$eCO_2RR$ to $CH_4$ involves complex proton-coupled electron transfer (PCET)[53]. The abundant supply of *H improves $eCO_2RR$ performance[54]. The Gibbs free energy of hydrogen (ΔGH) on Cu-$O_4$ SAC is -1.01 eV, which is 0.55 eV on Cu (111) and 1.60 eV on Cu-$N_4$ SAC [Figure 4D]. The more negative ΔGH on Cu-$O_4$ SAC signifies effortless H adsorption and effective inhibition of HER[54].

To evaluate the selectivity of methane by $eCO_2RR$ on Cu-$O_4$ SAC, the energetics of other products such as CO, HCOOH and $CH_3OH$ were calculated [Supplementary Figures 15-18] based on which the UL was derived. Specifically, the limiting potential ($U_L$) of $CH_4$ (-0.55 V) is much lower than that of CO (-2.01 V), CH3OH (-3.21 V), HCOOH (-4.07 V) [Figure 4E], indicative of its high selectivity towards $CH_4$. These discernible differences in UL underscore the significance of catalyst design in achieving the desired selectivity in electrocatalytic reactions. The outstanding activity and selectivity for methane formation on Cu-$O_4$ SAC, as revealed in DFT calculations, corroborates the electrochemical results.

## CONCLUSIONS

In summary, Cu SAC coordinated by four oxygen atoms were prepared by soaking Cu nanocubes on carbon support in acetic acid solution at 60 °C for 12 h. The dissolved Cu atoms from Cu cube were then captured by the oxygenated functional groups of the carbon substrate created during aqua regia treatment. The coordination structure was revealed by the EXAFS spectrum and XPS. Cu-$O_4$ SAC demonstrates an FE of 63.0% and partial current density of 200.5 mA $cm^{-2}$ towards methane production in $eCO_2RR$. Theoretical calculation indicates that the coordination structure of Cu-$O_4$ sites favors the strong hydrogen adsorption and hydrogenation of $eCO_2RR$ intermediates for methane production relative to that on Cu foil and Cu-$N_4$ SAC sites. The limiting potential calculation indicates that methane is energetically favored on Cu-$O_4$ sites compared to CO, methanol and formate. This study highlights the importance of regulating the coordination environment of SAC to steer the selectivity of $eCO_2RR$. The low-temperature synthesis method developed herein provides a practical and scalable approach for the preparation of structure-controlled SAC, advancing the design of efficient catalysts for sustainable energy applications.

## DECLARATIONS

### Acknowledgments

We appreciate the Shanghai Synchrotron Radiation Facility (SSRF) for help in XAS characterization.

### Authors' contributions

Writing - conceptualization, investigation, data curation, original draft: Qin, J.
Data curation, investigation, methodology, original draft: Hu, X.
Methodology, investigation, data curation: Miao, K.
Conceptualization, data curation, investigation, writing - review and editing, supervision, funding acquisition: Kang, X.

### Availability of data and materials

The raw data supporting the findings of this study are available within this Article and its Supplementary Materials. Further data is available from the corresponding authors upon reasonable request.

### Financial support and sponsorship

This work was supported by the National Natural Science Foundation of China (No. 22272059).

### Conflicts of interest

All authors declared that there are no conflicts of interest.

### Ethical approval and consent to participate

Not applicable.

### Consent for publication

Not applicable.



## REFERENCES

1. Liu, R. X.; Peng, L. W.; He, R. N.; Li, L. L.; Qiao, L. J. A high-performance continuous-flow MEA reactor for electroreduction $CO_2$ to formate. *J. Electrochem.* **2022**, *28*, 2104231. DOI
2. Zhuang, T.; Liang, Z.; Seifitokaldani, A.; et al. Steering post-C-C coupling selectivity enables high efficiency electroreduction of carbon dioxide to multi-carbon alcohols. *Nat. Catal.* **2018**, *1*, 421-8. DOI
3. Gu, Y.; Yang, J.; Wang, D. Electrochemical features of carbon prepared by molten salt electro-reduction of $CO_2$. *Acta. Phys-Chim. Sin.* **2019**, *35*, 208-14. DOI
4. Xiang, D.; Li, K.; Li, M.; et al. Theory-guided synthesis of heterostructured $Cu@Cu_{0.4}W_{0.6}$ catalyst towards superior electrochemical reduction of $CO_2$ to $C_2$ products. *Mater. Today. Phys.* **2023**, *33*, 101045. DOI
5. Wen, J.; Wan, Z.; Hu, X.; Huang, J.; Kang, X. Restructuring of copper catalysts by potential cycling and enhanced two-carbon production for electroreduction of carbon dioxide. *J. CO2. Util.* **2022**, *56*, 101846. DOI
6. Wan, Z. X.; Kuchkaev, A.; Yakhvarov, D.; Kang, X. W. Monodispersed Cu-TCPP/$Cu_2O$ hybrid microspheres: a superior cascade electrocatalyst towards $CO_2$ reduction to $C_2$ products. *J. Electrochem.* **2023**,. DOI
7. Zhang, H.; Wang, X.; Chen, C.; et al. Selective $CO_2$-to-formic acid electrochemical conversion by modulating electronic environment of copper phthalocyanine with defective graphene. *Chin. J. Struct. Chem.* **2023**, *42*, 100089. DOI
8. Birdja, Y. Y.; Pérez-gallent, E.; Figueiredo, M. C.; Göttle, A. J.; Calle-vallejo, F.; Koper, M. T. M. Advances and challenges in understanding the electrocatalytic conversion of carbon dioxide to fuels. *Nat. Energy.* **2019**, *4*, 732-45. DOI
9. Liu, M.; Peng, M.; Dong, B.; Teng, Y.; Feng, L.; et al. Explicating the role of metal centers in porphyrin-based MOFs of PCN-222(M) for electrochemical reduction of $CO_2$. *Chine. J. Struct. Chem.* **2022**, *41*, 2207046-52. DOI
10. Wang, Y.; Su, H.; He, Y.; et al. Advanced electrocatalysts with sngle-metal-atom active sites. *Chem. Rev.* **2020**, *120*, 12217-314. DOI
11. Miao, K.; Qin, J.; Yang, J.; Kang, X. Synergy of Ni nanoclusters and single atom site: size effect on the performance of electrochemical $CO_2$ reduction reaction and rechargeable Zn-$CO_2$ batteries. *Adv. Funct. Mater.* **2024**, *34*, 2316824. DOI
12. Qin, J.; Han, B.; Liu, X.; Dai, W.; Wang, Y.; et al. An enzyme-mimic single Fe-$N_3$ atom catalyst for the oxidative synthesis of nitriles via C-C bond cleavage strategy. *Sci. Adv.* **2022**, *8*, eadd1267. DOI
13. Fu, H.; Tian, J.; Zhang, Q.; et al. Single-atom modified graphene cocatalyst for enhanced photocatalytic $CO_2$ reduction on halide perovskite. *Chin. J. Catal.* **2024**, *64*, 143-51. DOI
14. Shi, G.; Xie, Y.; Du, L.; et al. Constructing Cu-C bonds in a graphdiyne-regulated Cu single-atom electrocatalyst for $CO_2$ reduction to $CH_4$. *Angew. Chem. Int. Ed. Engl.* **2022**, *61*, e202203569. DOI
15. Guan, A.; Chen, Z.; Quan, Y.; et al. Boosting $CO_2$ electroreduction to $CH_4$ via tuning neighboring single-copper sites. *ACS. Energy. Lett.* **2020**, *5*, 1044-53. DOI
16. Deng, Y.; Zhao, J.; Wang, S.; et al. Operando spectroscopic analysis of axial oxygen-coordinated single-Sn-atom sites for electrochemical $CO_2$ reduction. *J. Am. Chem. Soc.* **2023**, *145*, 7242-51. DOI
17. Wang, J.; Zhang, K.; Nga, T. T. T.; et al. Chalcogen heteroatoms doped nickel-nitrogen-carbon single-atom catalysts with asymmetric coordination for efficient electrochemical $CO_2$ reduction. *Chin. J. Catal.* **2024**, *64*, 54-65. DOI
18. Purbia, R.; Choi, S. Y.; Woo, C. H.; et al. Highly selective and low-overpotential electrocatalytic $CO_2$ reduction to ethanol by Cu-single atoms decorated N-doped carbon dots. *Appl. Catal. B:. Environ.* **2024**, *345*, 123694. DOI
19. Cai, Y.; Fu, J.; Zhou, Y.; et al. Insights on forming N,O-coordinated Cu single-atom catalysts for electrochemical reduction $CO_2$ to methane. *Nat. Commun.* **2021**, *12*, 586. DOI PubMed PMC
20. Dai, Y.; Li, H.; Wang, C.; et al. Manipulating local coordination of copper single atom catalyst enables efficient $CO_2$-to-$CH_4$ conversion. *Nat. Commun.* **2023**, *14*, 3382. DOI PubMed PMC
21. Yan, H.; Cheng, H.; Yi, H.; et al. Single-atom $Pd_1$/graphene catalyst achieved by atomic layer deposition: remarkable performance in selective hydrogenation of 1,3-butadiene. *J. Am. Chem. Soc.* **2015**, *137*, 10484-7. DOI
22. Hossain, M. D.; Huang, Y.; Yu, T. H.; Goddard, W. A. I. I. I.; Luo, Z. Reaction mechanism and kinetics for $CO_2$ reduction on nickel single atom catalysts from quantum mechanics. *Nat. Commun.* **2020**, *11*, 2256. DOI PubMed PMC
23. Liu, P.; Zhao, Y.; Qin, R.; Mo, S.; Chen, G.; et al. Photochemical route for synthesizing atomically dispersed palladium catalysts. *Science* **2016**, *352*, 797-800. DOI
24. Hu, R.; Li, Y.; Zeng, Q.; Shang, J. Role of active sites in N-coordinated Fe-Co dual-metal doped graphene for oxygen reduction and evolution reactions: a theoretical insight. *Appl. Surf. Sci.* **2020**, *525*, 146588. DOI

25. Fauzi, A.; Chen, X.; Zhao, H.; et al. Recent progress of M-N-C single atom electrocatalysts for carbon dioxide reduction reaction. *Next. Energy.* **2023**, *1*, 100045. DOI
26. Jin, M.; He, G.; Zhang, H.; Zeng, J.; Xie, Z.; Xia, Y. Shape-controlled synthesis of copper nanocrystals in an aqueous solution with glucose as a reducing agent and hexadecylamine as a capping agent. *Angew. Chem. Int. Ed. Engl.* **2011**, *50*, 10560-4. DOI
27. Segall, M.; Lindan, P. J.; Probert, M. A.; et al. First-principles simulation: ideas, illustrations and the CASTEP code. *J. Phys. Condens. Matter.* **2002**, *14*, 2717. DOI
28. Perdew, J. P.; Ernzerhof, M.; Burke, K. Rationale for mixing exact exchange with density functional approximations. *J. Chem. Phys.* **1996**, *105*, 9982-5. DOI
29. Perdew, J. P.; Burke, K.; Ernzerhof, M. Generalized gradient approximation made simple. *Phys. Rev. Lett.* **1996**, *77*, 3865. DOI PubMed
30. Vanderbilt, D. Soft self-consistent pseudopotentials in a generalized eigenvalue formalism. *Phys. Rev. B.* **1990**, *41*, 7892. DOI
31. Kresse, G.; Furthmüller, J. Efficiency of ab-initio total energy calculations for metals and semiconductors using a plane-wave basis set. *Comput. Mater. Sci.* **1996**, *6*, 15-50. DOI
32. Zhou, Y.; Wei, F.; Qi, H.; et al. Peripheral-nitrogen effects on the $Ru_1$ centre for highly efficient propane dehydrogenation. *Nat. Catal.* **2022**, *5*, 1145-56. DOI
33. Guo, C.; Zhang, T.; Deng, X.; et al. Electrochemical $CO_2$ reduction to $C_1$ products on single Nickel/Cobalt/Iron-doped graphitic carbon nitride: a DFT study. *ChemSusChem* **2019**, *12*, 5126-32. DOI
34. Lancet, D.; Pecht, I. Spectroscopic and immunochemical studies with nitrobenzoxadiazolealanine, a fluorescent dinitrophenyl analogue. *Biochemistry* **1977**, *16*, 5150-7. DOI PubMed
35. Lu, Z.; Chen, G.; Siahrostami, S.; et al. High-efficiency oxygen reduction to hydrogen peroxide catalysed by oxidized carbon materials. *Nat. Catal.* **2018**, *1*, 156-62. DOI
36. Liu, X.; Huang, L.; Ma, Y.; et al. Enable biomass-derived alcohols mediated alkylation and transfer hydrogenation. *Nat. Commun.* **2024**, *15*, 7012. DOI PubMed PMC
37. Song, P.; Hu, B.; Zhao, D.; et al. Modulating the asymmetric atomic interface of copper single atoms for efficient $CO_2$ electroreduction. *ACS. Nano.* **2023**, *17*, 4619-28. DOI
38. Zhang, X.; Xia, M.; Liu, T.; et al. Copper hexacyanoferrate as ultra-high rate host for aqueous ammonium ion storage. *Chem. Eng. J.* **2021**, *421*, 127767. DOI
39. Yang, F.; Ma, X.; Cai, W. B.; Song, P.; Xu, W. Nature of oxygen-containing groups on carbon for high-efficiency electrocatalytic $CO_2$ reduction reaction. *J. Am. Chem. Soc.* **2019**, *141*, 20451-9. DOI
40. Cheng, X. F.; He, J. H.; Ji, H. Q.; et al. Coordination symmetry breaking of single-atom catalysts for robust and efficient nitrate electroreduction to ammonia. *Adv. Mater.* **2022**, *34*, e2205767. DOI
41. Xie, C.; Lin, L.; Huang, L.; et al. Zn-$N_x$ sites on N-doped carbon for aerobic oxidative cleavage and esterification of C(CO)-C bonds. *Nat. Commun.* **2021**, *12*, 4823. DOI PubMed PMC
42. Rehr, J. J.; Albers, R. C. Theoretical approaches to x-ray absorption fine structure. *Rev. Mod. Phys.* **2000**, *72*, 621. DOI
43. Wang, Z.; Li, Y.; Zhao, X.; et al. Localized alkaline environment via in situ electrostatic confinement for enhanced $CO_2$-to-ethylene conversion in neutral medium. *J. Am. Chem. Soc.* **2023**, *145*, 6339-48. DOI
44. Wen, G.; Ren, B.; Wang, X.; et al. Continuous $CO_2$ electrolysis using a $CO_2$ exsolution-induced flow cell. *Nat. Energy.* **2022**, *7*, 978-88. DOI
45. Sinthika, S.; Vala, S. T.; Kawazoe, Y.; Thapa, R. CO oxidation prefers the eley-rideal or langmuir-hinshelwood pathway: monolayer vs thin film of SiC. *ACS. Appl. Mater. Interfaces.* **2016**, *8*, 5290-9. DOI PubMed
46. Fan, Q.; Zhang, M.; Jia, M.; Liu, S.; Qiu, J.; Sun, Z. Electrochemical $CO_2$ reduction to $C_{2+}$ species: heterogeneous electrocatalysts, reaction pathways, and optimization strategies. *Mater. Today. Energy.* **2018**, *10*, 280-301. DOI
47. Li, M.; Zhang, F.; Kuang, M.; et al. Atomic Cu sites engineering enables efficient $CO_2$ electroreduction to methane with high $CH_4/C_2H_4$ ratio. *Nanomicro. Lett.* **2023**, *15*, 238. DOI PubMed PMC
48. Jeon, S. S.; Kang, P. W.; Klingenhof, M.; Lee, H.; Dionigi, F.; Strasser, P. Active surface area and intrinsic catalytic oxygen evolution reactivity of NiFe LDH at reactive electrode potentials using capacitances. *ACS. Catal.* **2023**, *13*, 1186-96. DOI
49. Mao, X.; Wijethunge, D.; Zhang, L.; et al. Metal-free graphene/boron nitride heterointerface for $CO_2$ reduction: surface curvature controls catalytic activity and selectivity. *EcoMat* **2020**, *2*, e12013. DOI
50. Xun, W.; Yang, X.; Jiang, Q.; Wang, M.; Wu, Y.; Li, P. Single-atom-anchored two-dimensional $MoSi_2N_4$ monolayers for efficient electroreduction of $CO_2$ to formic acid and methane. *ACS. Appl. Energy. Mater.* **2023**, *6*, 3236-43. DOI
51. Guan, A.; Fan, Y.; Xi, S.; et al. Nitrogen-adsorbed hydrogen species promote $CO_2$ methanation on Cu single-atom electrocatalyst. *ACS. Mater. Lett.* **2023**, *5*, 19-26. DOI
52. Luo, Y.; Yang, J.; Qin, J.; et al. Cobalt phthalocyanine promoted copper catalysts toward enhanced electro reduction of $CO_2$ to $C_2$: synergistic catalysis or tandem catalysis? *J. Energy. Chem.* **2024**, *92*, 499-507. DOI
53. Zhou, L.; Lv, R. Rational catalyst design and interface engineering for electrochemical $CO_2$ reduction to high-valued alcohols. *J. Energy. Chem.* **2022**, *70*, 310-31. DOI
54. Chen, S.; Li, X.; Kao, C. W.; et al. Unveiling the proton-feeding effect in sulfur-doped Fe-N-C single-atom catalyst for enhanced $CO_2$ electroreduction. *Angew. Chem. Int. Ed. Engl.* **2022**, *61*, e202206233. DOI